# Thermal Modeling and Validation via Time-resolved Temperature Measurements for Nanosecond Laser Irradiation of a Powder Bed of Micro Metal Particles

Hanyu Song, Mengchen Wu, Weidong Liu, Benxin Wu\*

**Abstract:** Continuous-wave lasers (CW) are often used in selective laser sintering or melting; but short-pulsed lasers (e.g., with a pulse duration on the nanosecond scale) have their own potential advantages, such as high resolutions and small residual thermal effects. Compared with CW lasers, nanosecond lasers involve additional parameters (such as the pulse frequency) and more complicated relations between laser parameters and the powder bed thermal responses in laser sintering or melting. To help fundamentally understand the relations and guide efficient parameter selections, it is highly desirable to develop a thermal model for nanosecond laser irradiation of a metal powder bed and directly validate the model via in-situ transient temperature measurements. However, research work integrating such model development and validation has been rarely reported to the authors' best knowledge. In this paper, a thermal model has been developed for nanosecond laser irradiation of a powder bed of micro metal particles. The model-predicted transient surface temperature history of the powder bed agrees reasonably well with that measured by a fast pyrometry system. Under the conditions studied, the model simulations show that highfrequency nanosecond laser pulses can induce a significant thermal accumulation effect in a metal powder bed due to its lower thermal conductivity than that for a bulk metal. With the same timeaveraged laser power, by changing the pulse frequency, a nanosecond laser can induce very different temperature histories, melt pool evolutions and lifetimes, suggesting the laser has a potential advantage of good adjustability and flexibility in laser sintering. It also means a parameter-selection challenge due to the complicated parameter-thermal response relations. implying the importance of a thermal model validated by time-resolved temperature measurements.

**Keywords:** laser micro sintering, selective laser melting, selective laser sintering

#### 1. Introduction

Selective laser sintering or melting (SLS or SLM) is an important laser-based additive manufacturing process that can be used to make parts with short lead time and good flexibility in geometries and compositions (Selective laser melting typically refers to the process with full

\* Corresponding author: Benxin Wu, Associate Professor, School of Mechanical Engineering, Purdue University, 585 Purdue Mall, West Lafayette, IN 47907, USA, email: <a href="www.wu65@purdue.edu">ww65@purdue.edu</a>

melting of particles. In this paper, for simplicity "laser sintering" will be utilized to refer to all powder particle coalition process under laser irradiation regardless of the melting degree) [1, 2]. Continuous-wave lasers are often used in SLS or SLM [3-5]. On the other hand, pulsed lasers have their own potential advantages in selective laser sintering, such as high resolutions and small residual thermal effects. Research work has been reported in the literature on pulsed laser sintering, e.g., with laser pulse durations on the order of millisecond, microsecond or nanosecond [5-9]. In particular, short-pulsed lasers have been used in some reported research work on laser *micro* sintering, which often utilizes a powder bed filled with small particles of a few micrometers or less that could have a high achievable spatial resolution for the sintered micro features (e.g., [8, 9]). Among different types of short-pulsed lasers, nanosecond-pulsed lasers are often used (e.g., [8, 9]), which have the advantage of a good combination of strong robustness, low costs and reasonably short pulse durations.

Both CW and nanosecond (ns) lasers involve process parameters such as the laser beam wavelength, the average laser power ( $P_{ave}$ ) and the laser spot size on the powder bed surface. A ns laser involves additional parameters such as the pulse frequency (f) and pulse energy  $E_p$  (= $P_{ave}/f$ ), which could also significantly influence the powder bed thermal histories and temperature distributions during laser sintering. Hence, ns laser sintering can involve much more complicated relations between the laser parameters and the powder bed thermal histories (and/or temperature distributions) than those in CW laser sintering. To help fundamentally understand the relations and guide efficient parameter selections in ns laser sintering, it is highly desirable to develop a thermal model for the temperature evolution and distribution of the powder bed under nanosecond laser pulse irradiation, and then validate the model via in-situ time-resolved transient temperature

measurements. A model validation via time-resolved transient temperature measurements is highly desirable because it is a direct validation.

However, to the authors' knowledge such work integrating model development and validation via time-resolved transient temperature measurements has been rarely reported in the literature for a powder bed of micro metal particles under **nanosecond laser pulse** irradiation. Such a model validation is challenging because the transient temperature measurement for nanosecond laser pulse sintering often requires a much higher resolution in time than that for CW laser sintering or melting. Ref. [10] reported a thermal model for laser sintering with a CW laser beam irradiating a nickel powder bed with an average particle size of 25 µm. The laser-sintered widths predicted by the model were compared with those measured experimentally; but Ref. [10] did not report any model validation via transient temperature measurements. Ref. [11] reported numerical simulations of CW laser sintering of an iron powder layer and studied the effects of some process parameters; but it appeared that Ref. [11] did not show any direct model validation by experimental results. Refs. [12, 13] reported numerical models for nanosecond laser pulse interaction with a single spherical particle surrounded by a continuum (representing the surrounding powder), where the one-dimensional (1D) heat transfer equation was solved in the spherical coordinate system. It appeared that Ref. [12] did not show any experimental validation of the model, while Ref. [13] only discussed a qualitative comparison between model predictions and experimentally obtained micrographs of sintered materials. Ref. [14] reported a 2D axisymmetric numerical heat transfer/electromagnetic coupled model for nanosecond laser pulse sintering of bio-ceramic nanoparticles without showing model validation by experiments. Ref. [15] reported a model for femtosecond laser interaction with a single copper nanoparticle, where 1D two-temperature heat conduction equations were solved. The model simulation and the

experimental result show agreement on the laser fluence for multi-shot melting; but no comparison was made about the particle transient temperatures. Ref. [3] reported temperature measurements (but not a thermal model development or validation) for ns laser pulse sintering of titanium powder via an infrared camera, which, however, can only give time-averaged temperatures instead of the transient skin temperatures.

In a short summary, a thermal model for a powder bed of micro metal particles irradiated by nanosecond laser pulse that is validated by a direct comparison with time-resolved transient temperature measurements has been rarely reported to the authors' knowledge. As introduced earlier, such work of model development and validation is highly desirable. The purpose of the work in this paper is to develop a two-dimensional thermal model for nanosecond laser pulse irradiation of a powder bed of micro metal particles, and validate the model by comparing its predicted transient surface temperature history of the powder bed with that measured by a two-color fast pyrometry system. The pyrometry system was developed by the authors [16, 17], and it is based on a photodetector with fast responses. It is a non-contact measurement system that does not disturb the powder bed and does not need the value of the powder surface emissivity. After the experimental validation under the given condition, the model is used to perform simulations to help enhance the fundamental understanding of the powder bed thermal responses under nanosecond laser pulse irradiation, such as the effect of the laser pulse frequency.

Based on the model simulations, one main conclusion from this work is that even under the same average laser power, the adjustment of the nanosecond laser pulse frequency can dramatically change the powder bed thermal history, including the melt pool lifetime. This implies that laser sintering with a nanosecond laser is more adjustable and flexible in terms of the resulted material thermal history than a CW laser. Meanwhile, it also means that the laser-material interaction in nanosecond laser sintering can be much more complicated, suggesting the importance of a reasonably accurate, yet computationally efficient thermal model in the study and application of nanosecond laser sintering.

## 2. Model

As shown in Fig.1a, the model is a 2D axisymmetric model, where the powder bed surface is assumed to be located at z=0 and the powder bed is in the z>0 region. The thickness and radius of the computational domain in the powder bed is sufficiently large such that its bottom and side boundaries (i.e., the boundary at  $r=r_{max}$  and that at  $z=z_{max}$ ) do not obviously affect the simulation results under the conditions studied. The temperature at the bottom and side boundaries is assumed to be the initial room temperature (300 K). The nanosecond-pulsed laser beam propagates downwards in the +z direction with its central axis at r=0. It is assumed that the laser beam intensity follows a Gaussian distribution spatially, with a spot diameter on the powder bed surface equal to 160  $\mu$ m and a wavelength equal to 1064 nm. The cobalt powder bed is treated as a continuum medium with a porosity of  $\varepsilon$  and effective properties described later.

What will be simulated in this paper is the irradiation of the powder bed by multiple laser pulses with a pulse duration of ~200 ns per pulse, and the total simulated duration is up to a few hundred µs. Due to the short laser pulse duration and simulation time (and thus short melt pool lifetime), the melt flow is not considered in this model under the conditions studied. This approximate assumption can significantly simplify the model and greatly save the computational time. Whether or not this can still lead to reasonably good accuracy in the temperature prediction will be checked by comparing it with the experimental measurement as shown later. With this

assumption, the heat transfer process in the powder bed is governed by the following twodimensional (2D) axisymmetric heat transfer equation [18, 19]:

$$\frac{\partial \rho H}{\partial t} = \frac{1}{r} \left[ r k_{eff} \frac{\partial^2 T}{\partial r^2} + \frac{\partial T}{\partial r} \frac{\partial}{\partial r} (k_{eff} r) \right] + \frac{\partial}{\partial z} \left( k_{eff} \frac{\partial T}{\partial z} \right) + \left( -\frac{\partial I(r,z,t)}{\partial z} \right) \tag{1}$$

where t is time, r and z are spatial coordinates (where the +z direction points into the powder bed), T is temperature, H denotes the material enthalpy per unit mass that depends on the temperature, specific heat and also latent heat of melting (for melted material),  $k_{eff}$  represents the effective thermal conductivity of the medium in the powder bed, I is the net laser beam intensity propagating in +z direction in the powder bed, and  $\rho$  is the medium density and is given by  $\rho = \rho_b(1-\varepsilon) + \varepsilon \rho_a$ , where  $\rho_b$  and  $\rho_a$  are the density of the bulk metal (cobalt) and the argon (assumed to fill the pores), respectively, and  $\varepsilon$  is the medium porosity. The value of the term,  $\varepsilon \rho_a$ , is very small and hence has been neglected. In the relation curve of H(T) versus T, the slope is the corresponding bulk metal specific heat in the range of  $T < T_m - \delta T$  and the range of  $T > T_m + \delta T$ , where  $T_m$  is the melting point. For the temperature range  $[T_m - \delta T, T_m + \delta T]$ , the slope is  $L_m/(2\delta T)$ , where  $L_m$  is the latent heat of melting and  $\delta T$  is a small value (which is chosen to be 0.5 K in the calculations in this paper). During the material heating process, melting starts when the temperature reaches  $T_m - \delta T$ . Argon is neglected in constructing the H versus T relation because of its much smaller density than that for the metal.

The last term on the right side of Eq.(1) is the volumetric heat source term due to the absorption of the energy of laser beam penetrating into the surface layer of the powder bed. If it is assumed that z = 0 is located at the powder bed surface and the +z direction points into the bed, then the net laser beam intensity propagating in the +z direction at a certain location (r, z) within the powder bed can be calculated by [20]:

$$I(r,z,t) = I_0(r,t) \left\{ -\frac{(1-R-a)[3c+2R(1-h-c)]}{(1-h)(1-4a^2)\exp(2abz)} - \frac{(1-R)[1-4R(h-c)]+2a^2}{(1-4a^2)\exp(bz)} \right\}$$
 (2)

where  $I_0(r,t)$  is the incoming laser beam intensity at the powder bed surface that is approximately assumed to follow a Gaussian distribution, R is the material hemispherical reflectance at 1064 nm, h and c are constants (h = 1/3 and c = 1/6 for diffuse reflection),  $a^2 = 1 - 2hR - R^2(1 - 2h)$ , and  $b = \pi r_0^2 n/\varepsilon$ , where  $r_0$  is the particle radius, n is the number of particles per unit volume and is related to the porosity  $\varepsilon$  by:  $\varepsilon = 1 - 4\pi r_0^3 n/3$ . Based on Eq. (2), the last term on the right side of Eq.(1) can be calculated.

The effective thermal conductivity of the powder bed medium can be significantly different from that for the bulk metal. In Ref. [21], the effective thermal conductivities for a solid powder bed of micro iron particles at different porosities have been determined by numerically simulating the heat transfer process in the powder bed with stochastically filled particles. It has been found that at a porosity level near  $\sim 0.72$  (which is the measured solid powder bed porosity for the study in this paper), the effective thermal conductivity of the iron powder bed in the air environment is approximately ~3% of that for the bulk iron. Solid cobalt is a metal with a regular density, thermal conductivity and specific heat reasonably similar to those for solid iron [21-24]. The thermal conductivity and diffusivity of regular air [25] are also reasonably similar to those for argon [26, 27]. Hence, in the model in this paper, it has been approximately assumed that for the solid powder bed medium,  $k_{eff} = 0.03k_{b,s}$ , where  $k_{b,s}$  is the thermal conductivity of the solid bulk cobalt. For the melted powder bed medium region, the effective thermal conductivity is approximately calculated using the simple rule of mixtures given by  $k_{eff} = (1 - \varepsilon)k_{b,l} + \varepsilon k_a$  [19, 28], where  $k_{b,l}$  is the bulk cobalt thermal conductivity in the liquid state and  $k_a$  is the argon conductivity. For the powder bed medium that has an enthalpy in the partial melting range, the effective thermal

conductivity is obtained through a linear interpolation (based on the temperature) between the solid value at  $T_m - \delta T$  and the melted medium value at  $T_m + \delta T$ . For melted and then re-solidified material, the effective thermal conductivity is also approximately calculated using the aforementioned simple rule of mixtures based on the solid bulk cobalt conductivity without considering the argon contribution due to its much smaller conductivity.

The powder bed is assumed to be at the room temperature (300 K) initially. As introduced earlier, the computational domain is chosen to be sufficiently large such that the bottom and side boundaries can be assumed to remain at the room temperature for the simulated durations in this paper. For the powder bed top surface at z = 0, the heat loss due to the possible surface vaporization process is considered. The surface vaporization flux can be approximately calculated by the Hertz-Knudsen equation with the saturated vapor pressure calculated by the Clausius-Clapeyron equation, which leads to the following boundary condition at z = 0 [18, 29-31]:

$$k_{eff} \frac{\partial T}{\partial z} = L_{vap} \beta P_b \exp\left[\frac{L_{vap} m}{k_b T_b} \left(1 - \frac{T_b}{T_s}\right)\right] \sqrt{\frac{m}{2\pi k_b T_s}}$$
(3)

where  $L_{vap}$  is the latent heat of vaporization,  $\beta$  is the vaporization coefficient (=~0.82 based on more detailed Knudsen layer relations assuming Mach number is 1 right above the Knudsen layer [18, 30]),  $P_b$  is the saturated vapor pressure at the temperature  $T_b$  (which is the normal boiling point when  $P_b = 1$  atm),  $k_b$  is the Boltzmann constant, m is the molecular mass, and  $T_s$  is the powder bed surface temperature. In Eq.(3), only the latent heat of vaporization consumed is considered because it is expected to dominate over the other energy components (such as the energy raising the material temperature to  $T_s$  including the latent heat of melting before it is vaporized). The effect of the vaporization-induced material loss and surface receding on the heat transfer process in the powder bed is neglected, because under the conditions simulated in this paper the vaporized

material amount, if any, has been found to be typically very small. Other heat losses from the top surface, such as those via thermal radiation and surface convection, are also neglected in the model. As discussed later, the effects of these heat losses on the calculated temperatures are very small.

The initial powder bed medium porosity is estimated to be ~0.72 based on the measured apparent density of the powder placed into the powder bed. The nominal particle size for the cobalt powder used in the experimental work in this paper is ~1.6 µm according to the product specification (Alfa Aesar, Product number: 10455). However, the particles in the powder bed could have agglomerations, increasing their effective sizes. The powders used in the experiment in this paper are the same as those in the authors' previous paper [17]. The cross-sectional scanning electron microscope (SEM) image in Fig.4a of Ref.[17] shows a region of powder particles below the densely sintered layer. Based on this region of the SEM image, the effective particle diameter has been roughly estimated with the ImageJ software [32] to be ~2.56 μm (the particles used are not in a spherical shape. This estimated value is the diameter of an "equivalent" spherical particle that would have the same average area in the cross-sectional image). This value is used in the calculation with Eq.(2) for the solid powder bed medium. The total simulated durations are very short (typically only a few hundred us) in this study for nanosecond laser pulse irradiation of the metal powder bed. Solid state sintering (if occurs at all) is not explicitly considered in the model. Upon full melting (i.e., when the temperature reaches  $T_m + \delta T$ ) the local medium effective density p is approximately assumed to remain the same, and then the updated porosity for the melted medium can be determined based on the difference between the solid and liquid bulk cobalt densities. Assuming the number of particles per unit volume remains the same, the updated effective particle diameter for the melted medium can also be obtained. The porosity of the medium in the temperature range of  $[T_m - \delta T, T_m + \delta T]$  is determined via a linear interpolation based on

the solid medium porosity at  $T_m - \delta T$  (which is 0.72) and the melted medium porosity at  $T_m + \delta T$ .

The process of the laser pulse interaction with the powder bed is very complicated. The model in this paper, which is based on the aforementioned approximate and/or simplified assumptions, has a relatively low computational cost, which is very desirable in many situations. The model has a relatively low computational cost because it does not explicitly simulate the possible melt flow, or the evolutions of individual particles (which would lead to an extremely high computational cost due to the small particle size). The model cannot strictly calculate the porosity evolution and its major goal is to simulate the temperature evolution of the powder bed. The model will be tested by comparing its predicted transient surface temperature history with that measured experimentally.

The heat transfer equation in the model is solved numerically by an explicit finite difference method [33]. A non-uniform mesh is used in the model calculations. For most of the results in the paper, unless otherwise indicated, the smallest mesh size occurs at r=z=0, where  $\Delta r=0.25~\mu m$ , and  $\Delta z=0.15~\mu m$ . The values of  $\Delta r$  and  $\Delta z$  gradually increase with the coordinate r and z, respectively. Then, constant mesh sizes of  $\Delta r=0.65~\mu m$  and  $\Delta z=0.4~\mu m$  are use in the range of  $20\mu m < r < 60\mu m$  and  $5\mu m < z < 20\mu m$ , respectively. Beyond this range, the mesh sizes continue increasing again. Typically, around ~17150 grid points are used in the computational domain. The model calculations are based on a code developed by the authors using MATLAB (version R2020b. The MathWorks, Inc.).

The major material properties used in the simulation, such as bulk cobalt densities, specific heats, latent heats of melting and vaporization, normal melting and boiling points, bulk cobalt thermal conductivities, and cobalt index of refraction are taken from the literature [24, 27, 34-39]

(see Table 1). For the bulk cobalt density  $\rho_b$ , a constant value (8.85 g/cm<sup>3</sup>) is used for the solid state (which is the density for close-packed hexagonal cobalt at 20 °C) [24] and a different constant value (7.75 g/cm<sup>3</sup>) is used for the liquid state [34]. The cobalt specific heat is obtained based on [35] as described in Table 1 of this paper. The temperature-dependent bulk cobalt thermal conductivity in the solid state,  $k_{b,s}$ , and that in the liquid state,  $k_{b,l}$ , are taken from Refs. [36] and [37], respectively. In the simulation, the value of  $k_{b,s}$  is determined via a linear interpolation using the first data point and the data point at 1000 K for pure cobalt given in Fig.3 of Ref.[36] (in the figure, the conductivity value for the last data point at a temperature a little higher than 1000 K is reasonably close to that at 1000 K and hence is not used). For the temperature range of 1000 K to  $T_m - \delta T$ , the conductivity value at 1000 K from [36] is used for  $k_{b,s}$ . In Table 6 of Ref. [37], the thermal conductivity of bulk liquid cobalt in the range of 1800 K to 1950 K is given. In the simulation, for bulk liquid cobalt below 1800 K and that above 1950 K, the conductivity value at 1800 K and 1950 K from [37] is used, respectively, for  $k_{b,l}$ . Based on the solid and liquid bulk cobalt thermal conductivities,  $k_{b,s}$  and  $k_{b,l}$ , the corresponding powder bed medium effective thermal conductivity,  $k_{eff}$ , can be calculated in the way as introduced earlier. The argon thermal conductivity is taken from Table 1 of [27] (The last column for 70.0 cm Hg of the table is used. The conductivity at temperatures below the minimum or above the maximum temperatures in the table is assumed to be equal to that at the minimum and maximum temperatures, respectively). The optical index of refraction of solid and liquid cobalt at 1064 nm are determined based on the dielectric constants from Fig.6 of Ref. [38] and Table III of Ref. [39] (the value from [39] at the melting point and  $\lambda = 1.06 \mu m$  is used for liquid cobalt), respectively, based on which the corresponding hemispherical reflectance, R, can be calculated [40, 41], which is then used in Eq.(2). The value of R in the temperature range of  $[T_m - \delta T, T_m + \delta T]$  is determined via a linear

interpolation using the solid value at  $T_m - \delta T$  and the liquid value at  $T_m + \delta T$ . The latent heat of melting and vaporization, normal melting and boiling points for cobalt are taken from Table 1 of Ref. [24].

It should be noted that although the melting point of a metal particle may decrease as its size decreases, typically such an effect is obvious only when the particle size is very small. When the particle size reaches the scale of several hundred nanometers, the melting point is typically close to the bulk melting point. For example, Fig.9 of Ref. [42] implies that when the radius of Fe, Cr, Mo and W particles reaches several hundred nanometers, their melting points should be very close to the bulk values. It is expected that this should also be the case for cobalt particles. Hence, the bulk cobalt melting point is used in this paper.

## 3. Experimental Setup

Figure 1b shows the experimental setup for nanosecond laser pulse irradiation of a powder bed of metal (cobalt) micro particles, including a two-color fast pyrometry system for time-resolved temperature measurements that will be used to validate the model developed.

The powder bed contains cobalt powder (Alfa Aesar, Product number: 10455). The powder bed lateral dimensions and the powder layer thickness are sufficiently large such that the effects of the powder layer side and bottom boundaries on the measured temperatures are insignificant. The powder particles are applied into the powder bed using a doctor blade after first being moistened with 95% ethanol. The particles get naturally dried before the experimental measurements. It is expected that the amount of residual ethanol in the powder bed, if any at all, will be very small and does not have a significant effect on the measured temperatures in this paper. In each experiment, the laser (SPI G3.0) sends out a train of 10 pulses onto the surface of

the powder bed at a pulse frequency of 25 kHz (thus the distance in time between neighboring pulses is 40  $\mu$ s), with an average pulse energy of ~0.14 mJ/pulse. Each pulse typically has a full pulse duration of ~200 ns and a temporal shape similar to that shown in the corresponding author's previous paper [43]. The laser beam has a wavelength of ~1064 nm and an approximately Gaussian intensity profile. The beam is stationary during each experiment and is focused by the lens of a 100-mm focal length inside the scan head (HurryScan 14 from ScanLab). The powder bed surface is at a vertical location such that the laser spot diameter on the surface is approximately ~160  $\mu$ m, which is measured by the knife-edge method. After each experiment, the laser spot will be moved to a new location of the powder bed and another 10 laser pulses will be fired to the location. The measured transient temperature history of the powder bed surface is based on multiple measurements under the same laser condition. The powder bed is inside a chamber with a top glass cover. Before each experiment, argon is slowly flown into and out of the chamber for some time. During each experiment, the argon flow continues, but an opening is left for the top glass cover to facilitate the experiment.

The two-color fast pyromery system shown in Fig.1b is a system developed by the authors and is similar to that in the authors' previous papers [16, 17], where more details can be found. In this paper, only a short introduction will be given about the system, including some specific details that could be different from those in the previous papers. In [16], a similar pyrometry system was used for in-situ temperature measurements during CW laser sintering of carbon nanotube-reinforced silver matrix composite thin films on a polymer substrate, while in [17], a similar pyrometry system was used for temperature measurements in an experimental study for single-track laser micro sintering using nanosecond laser pulses. It should be noted that neither Ref. [16] nor Ref. [17] involves model **development or validation** work for nanosecond laser pulse

irradiation of a powder bed of micro metal particles, which is the focus of the work presented in this paper.

The pyrometry system determines the transient temperature of the powder bed surface by measuring the thermal radiation emitted from the surface (mainly from a small "measurement spot" region) in two different wavelength ranges. As shown in Fig.1b, the radiation is collected by the objective (MY10X-823, 10X Mitutoyo Plan Apochromat Objective, purchased from Thorlabs; NA = 0.26, effective focal length = 20 mm), after which the radiation will reach a switchable long pass filter from Thorlabs that blocks most radiation below a certain cut-on wavelength. The filter can have a cut-on wavelength of either 1200 nm or 1400 nm, which is called a Type A or Type B filter, respectively. After passing through the filter, the remaining radiation (mainly above the cuton wavelength) is focused by a lens onto the photodetector (Thorlabs PDA015C/M), which has a measurable wavelength range up to ~1800 nm based on its responsivity curve given in the product user guide. The photodetector converts radiation power into a photocurrent, which then induces a voltage signal being measured by an oscilloscope with a sampling frequency of 50 MHz. Multiple experiments are performed using Type A and Type B filters in the system, respectively, which measure the radiation in the wavelength range of ~1200 nm to ~1800 nm and the range of ~1400 nm to ~1800 nm, respectively.

The voltage signals obtained with Type A filter from multiple measurements will be averaged. The mean dark voltage of the photodetector is subtracted from the averaged signal, which then passes through a 4<sup>th</sup> order Butterworth low-pass filter in Matlab (with a cutoff frequency of 0.14, normalized by half of the sampling frequency of the oscilloscope) to decrease high-frequency noise, leading to a voltage signal of  $V_A(t)$ . Similarly, with Type B filer, the voltage signal  $V_B(t)$  can be obtained. The portion of  $V_B(t)$  that is below two times the oscillation amplitude

of the photodetector dark voltage will be truncated, because this portion is deemed to be insufficiently reliable for temperature deduction. Then, the signal  $V_A(t)$  is truncated accordingly to make its duration the same as that for  $V_B(t)$ . As derived and shown in the authors' previous papers [16, 17], the ratio of the two voltage signals has the following relation:

$$\frac{V_A}{V_B} = \frac{\int_{1200 \ nm}^{1800 \ nm} \theta(\lambda) T_r(\lambda) \frac{2h'c_0^2}{\lambda^5 \left[ \exp\left(\frac{h'c_0}{\lambda k_b T}\right) - 1 \right]} d\lambda}{\int_{1400 \ nm}^{1800 \ nm} \theta(\lambda) T_r(\lambda) \frac{2h'c_0^2}{\lambda^5 \left[ \exp\left(\frac{h'c_0}{\lambda k_b T}\right) - 1 \right]} d\lambda} \tag{4}$$

where h' and  $k_b$  represent the Planck and Boltzmann constants, respectively,  $c_0$  denotes the vacuum light speed,  $\theta$  is the photodetector responsivity and the relation of  $\theta$  versus the wavelength  $\lambda$  is given in the user guide for the photodetector, and  $T_r$  denotes the total optical transmission of all the optical elements in the radiation propagation path prior to the photodetector, the variation of which with  $\lambda$  can be determined based on the wavelength-dependent transmission of each individual element (including the objective) that can be found in the product information of the element from the corresponding vendor.

In deriving Eq.(4), one effective temperature T(t) is assumed for the entire measurement spot at any instantaneous moment t. The measurement spot is approximately an ellipse with a size of roughly  $\sim 50 \times \sim 70 \,\mu m$  based on an estimation similar to that described in Ref.[16] (which also gives a detailed introduction about the definition of the measurement spot). The measurement spot center is aligned to approximately overlap with the laser spot center on the powder bed surface. It has also been approximately assumed that the wavelength dependence of the powder bed surface spectral, directional emissivity (in the angle range around  $45^{\circ}$  involved in the measurement) can be approximately neglected in the wavelength range of 1200 to 1800 nm. In [17], this approximate assumption has been theoretically analyzed to be reasonable at multiple high temperatures in the

range of 1400 to 3000 K (for the angles of 45° and 45°  $\pm$  16°) based on the Kirchhoff's law, Fresnel equations and the Drude model. More details can be found in Ref.[17].

In the authors' previous paper [16], a validation of a similar pyrometry system and approach (at least to a certain extent under the given condition in [16]) is demonstrated, where the silver melting duration of a laser-irradiated target (a thin-film mixture of silver nanoparticles and carbon nanotubes) determined via the pyrometry system agrees well with that determined by measuring the target-reflected light of a probe laser beam.

#### 4. Results and Discussions

Figure 2 shows the comparison between the model prediction and the experimental measurement for the measurement spot temperature. From the measurement result, it can be seen that the temperature quickly rises to a local peak value and then starts dropping. However, the next laser pulse arrives when the temperature is still at an elevated value, and the temperature is driven to another local peak that is typically higher than the previous one (except for the last a few pulses). This pattern repeats until the last laser pulse, after which the temperature will decrease. Thus, the measurement result suggests a thermal accumulation effect between neighboring laser pulses in time under the condition studied. As introduced earlier, the portion of  $V_B(t)$  that is below two times the oscillation amplitude of the photodetector dark voltage is truncated, because this portion is deemed to be insufficiently reliable for temperature deductions. Hence, only temperatures sufficiently high can be measured by the pyrometry system. The portion of the measured temperature curve for the 1st laser pulse is not very complete due to a poor signal quality, which is likely due to the relatively low temperatures in the related period.

Figure 2 also shows the model prediction for the measurement spot temperature. As introduced earlier, from the in-situ temperature measurement with the pyrometry system, at any given instantaneous moment t, only one temperature can be obtained for the measurement spot, which is approximately an ellipse of  $\sim 50 \times \sim 70 \,\mu m$ . On the other hand, the model calculation can predict a spatial distribution of the temperature of the powder bed surface T(r, 0, t). Hence, to make the comparison between the model prediction and the experimental measurement meaningful, a spatially average temperature  $T_{ave}(t)$  is calculated for the measurement spot based on the modelpredicted temperature distribution T(r, 0, t). Two extreme ways of calculating the average temperature is: (1) the simple spatially average temperature,  $T_{ave}(t) = \int T(r, 0, t) dA/A$ , where A is the measurement spot area, and (2) the weighted spatially average temperature using  $T^4$  as the weight considering that the measured temperature is based on the thermal radiation emitted from the powder bed surface and the hotter region typically has a higher power of the emitted thermal radiation per unit area:  $T_{ave}(t) = \left[\int T(r,0,t) \cdot T^4(r,0,t) dA\right] / \left[\int T^4(r,0,t) dA\right]$ . It has been found that for the studied case the average temperature obtained using the two different approaches turn out to be typically close. Hence,  $T_{ave}(t)$  calculated using the second, weighted approach is plotted in Fig.2 as the model-predicted temperature for the measurement spot.

From Fig.2, it can be seen that overall the model-predicted temperature history curve agrees reasonably well with the measured one under the given condition. Similar to that suggested by the measurement result, the model simulation result has also shown the thermal accumulation effect between neighboring laser pulses. Typically the peak temperature after each laser pulse increases with the number of pulses. For most of the laser pulses, the model-predicted temperature peaks are reasonably close to those from the measurement. The reasonably good agreement suggests that the accuracy of the relatively simple and low computational cost model should be

sufficient to be used for a *meaningful* (although not necessarily fully accurate in the quantitative sense) study of process parameter effects, which will be introduced later.

On the other hand, some differences between the model prediction and the experimental measurement can be seen in Fig. 2, particularly in the falling portions of the curve. It is expected that one major reason for the differences could be that the value of the effective thermal conductivity used in the model for the high-temperature solid powder bed region is smaller than the actual value. It is still challenging to obtain reliable values for the effective thermal conductivities of solid metal powders at very high temperatures, which could be affected by many factors. On the one hand, theoretically calculated or estimated thermal conductivities could have deviations from the actual values. On the other hand, the experimental measurement work for solid metal powder conductivities at very high temperatures (e.g., > ~1000 K) has been limited. Refs.[44] and [45] have reported experimental measurements of solid metal powder thermal conductivities at elevated temperatures, but the temperatures are only up to 473 K and 500 °C, respectively. Future work to obtain reliable solid metal powder thermal conductivities at very high temperatures would certainly be desirable, which could also help improve the accuracy of the thermal model in this paper. However, as discussed earlier, the model-experiment agreement shown in Fig.2 is already reasonably good under the given condition, which suggests that the model accuracy should be sufficient for a meaningful study of process parameter effects, which will be introduced later.

Figure 3 shows the model-predicted temperature profiles in the r-z plane at different moments. It can be seen that right after the end of the 9<sup>th</sup> and 10<sup>th</sup> laser pulse, the melt pool dimensions and the temperatures in the hot powder bed region are obviously larger or higher than those at the moment right before the 9<sup>th</sup> and 10<sup>th</sup> laser pulse, respectively. In other words, the

irradiation of the powder bed by the laser pulses with the 40- $\mu$ s pulse-to-pulse separation time has created an oscillating melt pool. This can be seen more clearly in Fig.4, which shows that the melt pool depth (at the laser spot center) oscillates with time and the peak value in each cycle increases with time. The total accumulated melt pool lifetime of the powder bed surface at the laser spot center is ~279  $\mu$ s, which is much longer than the total pulse duration of the 10 laser pulses. It should be noted that when plotting Figs. 3 and 4, the melt pool boundary is defined as the location with  $T = T_m$ .

As introduced earlier, the convection and thermal radiation heat loss from the powder bed surface has been neglected in the model. It has been found that if the thermal radiation loss is added (using its upper limit value of  $\sigma T^4$ , where  $\sigma$  is the Stefan-Boltzmann constant [46]) and the heat convection loss is added using a convection coefficient value of  $h_c = 25 \text{ W/(m}^2 \text{ K})$  taken from [10], then the model-predicted temperature history of the powder bed surface does not have any obvious change from that in Fig.2. In the model, possible surface vaporization has been considered in an approximate way using the Hertz-Knudsen equation, without solving the gas dynamic equations for the vapor and ambient gas phase. Under the conditions studied, it has been found that the amount of vaporized material is small. Hence it is expected that the vaporization-induced surface receding effect can be approximately neglected for the powder bed. The possible melt flow in the powder bed is not considered in the model, and this has greatly saved the computational cost, which is highly desirable in many situations. The reasonably good model-experiment agreement shown Fig. 2 suggests that this simplified assumption of the model does *not* cause significant inaccuracy in predicting the measurement spot temperature under the given condition. On the other hand, the possible actual melt flow towards the surrounding porous powder bed medium could enlarge the melted region radius observable by a microscope after the laser pulse irradiation. This

could cause an under-prediction of the maximum melt pool radius on the powder bed surface by the model. This is consistent with the post-process microscopic observation showing that the model has under-predicted the maximum melted region radius by around  $\sim\!25~\mu m$  under the given condition for Fig.2.

Compared with CW laser sintering, nanosecond laser pulse sintering involves more laser parameters. One important parameter is the laser pulse frequency, which is the number of pulses fired per unit time. Under the same time-averaged laser power, a higher laser pulse frequency means a lower pulse energy and a shorter pulse-to-pulse distance in time. Even with the same timeaveraged laser power, the thermal responses of the powder bed irradiated by nanosecond laser pulses can be very different under different laser pulse frequencies. This can be seen from Fig.5, which shows the powder bed surface temperature histories at the laser spot center under the irradiation of laser pulses fired with different pulse frequencies in the period of t = 0 to 400 µs. For this 400-µs period, all the simulated cases shown in Fig.5 have the same time-averaged laser power and thus the same total laser energy input, which also means the same value of pulse number x energy/pulse. For the period of t = 0 to 400  $\mu$ s, with the pulse frequencies of 5, 12.5, 25 and 100 kHz, the number of laser pulses fired is 2, 5, 10 and 40, respectively. The energy per pulse decreases as the pulse frequency increases. In addition, Fig.5 also shows the simulation result for one single laser pulse with a duration of 400 µs with a top-flat temporal shape, which has the same time-averaged power as that for the 200-ns laser pulses for the period of t = 0 to 400  $\mu$ s. Figure 6 shows the histories of the melt pool depths for the same simulated cases as those in Fig. 5, while Figure 7 shows the total melt pool lifetimes at the laser spot center on the powder bed surface for different laser pulse frequencies.

Figs. 5 to 7 shows that even with the same time-averaged laser power and total laser energy input, laser pulses fired with different frequencies have induced dramatically different thermal responses (e.g., surface temperature histories, melt pool evolutions and lifetimes) for the powder bed. The low-frequency and high-energy (per pulse) laser pulses fired at 5 kHz generate very high transient peak temperatures, which means that they can easily melt the metal (or another type of metal with a much higher melting point); but the pulse-to-pulse distance in time is large and hence the thermal accumulation effect is relatively weak (but certainly still exists). Figure 5a shows that the temperature drops to ~993 K when the second laser pulse is fired, and the peak temperature generated by the second laser pulse is close to that by the first pulse. Figure 6a shows that the melt pool depth has dropped to 0 before the second laser pulse comes, and the peak pool depth generated by the second laser pulse is  $\sim$ 4.5  $\mu$ m deeper than that by the first pulse. The total melt pool lifetime is relatively low (~162 µs) as shown in Fig.7. On the other hand, Fig.5 shows that the highfrequency low-energy laser pulses fired at 100 kHz induce much lower temperature increase per pulse; but the short pulse-to-pulse distance in time causes a very significant thermal accumulation effect. Hence, eventually the powder bed surface can still be melted, and the melt pool depth evolution is shown in Fig.6b. The total melt pool lifetime is ~279 µs, much longer than that by the 5 kHz laser pulses, as shown in Fig. 7. Fig. 5b and 6b show that the surface temperature history and the melt pool depth evolution induced by the 100-kHz ~200-ns-duration laser pulses are similar to those by the single top-flat 400-µs laser pulse (which can also be regarded as a "CW" laser that is on for 400 µs). To accurately calculate the transient melt pool depth evolution, the mesh used in the simulations for the cases in Fig.5b and 6b is slightly different from that for the other cases in this paper. A larger number of grid points ( $\sim$ 25900) is used, and  $\Delta z$  is equal to 0.2  $\mu$ m in the range of  $2\mu m < z < 15\mu m$ , and  $\Delta z$  continues increasing gradually for  $z > 15 \mu m$ .

In a short summary, the results in Figs.5 to 7 show that even with the same time-averaged laser power and total laser energy input, by changing the laser pulse frequency, the ~200-ns duration laser pulses can induce significantly different temperature histories, melt pool evolutions and lifetimes, ranging from a very high transient peak temperature (which can easily melt a high-melting-point material) at a low pulse frequency, to a temperature history at a high pulse frequency similar to that induced by a much longer 400-µs laser pulse. This suggests the great adjustability and flexibility by nanosecond laser pulses for laser sintering, which is a potential great advantage. On the other hand, this also means a very complicated relation between laser parameters and the induced thermal responses in the powder bed, which is a challenge in parameter selections and optimizations, implying the importance and value of a thermal model validated by time-resolved temperature measurements.

One reason for the complicated thermal responses induced by nanosecond laser pulses at different pulse frequencies shown in Figs.5 to 7 is the thermal accumulation effect between adjacent pulses, to which one major contributing factor is the relatively low thermal conductivity of the powder bed compared with that for a bulk metal. The laser-induced thermal responses can become much less complicated for a bulk metal, which typically has a much higher thermal conductivity. This can be seen from Fig.8, which shows the surface temperature histories at the laser spot center for a bulk cobalt irradiated by 25 kHz and 100 kHz ~200-ns-duration laser pulses as well as that by one single 400-µs-duration pulse. Laser parameters are the same as those in the corresponding cases in Fig.5. As shown in Fig.8, due to the high thermal conductivity of the bulk cobalt, no obvious thermal accumulation effect is seen even with a high laser pulse frequency of 100 kHz. After the beginning of each laser pulse, the temperature quickly increases to a peak value and then quickly drops to around the room temperature before the next laser pulse comes. Then a

similar temperature history will repeat for each and every following laser pulse. The laser-induced peak temperature is higher at the lower pulse frequency of 25 kHz, but still does not reach the melting point yet. The temperature increase induced by the single 400- $\mu$ s-duration pulse is very small. It should be noted that the plotting of the model-predicted temperature history curves shown in Figs. 2, 5 and 8 may or may not start from the exact moment of t = 0. In the model simulations for the bulk metal target, the surface reflectivity for the perpendicularly incident laser beam is calculated based on Fresnel equations [41] for a flat surface using the cobalt complex index of refraction at 1064 nm. The absorbed laser power density is treated as a surface heat flux when solving Eq.(1). The reflectivity value in the temperature range of  $[T_m - \delta T, T_m + \delta T]$  is determined via a linear interpolation using the solid value at  $T_m - \delta T$  and the liquid value at  $T_m + \delta T$ .

Refs. [29, 47, 48] reported thermal models for nanosecond laser irradiation of bulk targets, which are also based on a heat transfer equation in the target. Different from these models, the thermal model in this paper is for a powder bed instead of a bulk target (except for the results in Fig.8). The model has considered the effect of powder porosity on the target medium effective density and thermal conductivity. In addition, the models in Refs. [47, 48] use the bulk target surface reflectivity and optical absorption coefficient to calculate laser energy deposition in the target, and the model in Ref.[29] treats the absorbed laser beam power per unit area as a surface heat flux. On the other hand, in the model in this paper, Eq. (2) is applied to calculate the laser beam propagation and energy absorption in a powder medium for the situation studied in this paper, where the laser pulse has a relatively long duration of ~200 ns among different types of nanosecond lasers. It should also be noted that Refs.[29, 47, 48] did NOT verify the model-

calculated target surface temperatures via direct comparisons with in-situ time-resolved measurements of the temperatures, while this has been performed in this paper.

#### 5. Conclusions

Research work integrating thermal model development and validation via time-resolved transient temperature measurements has been reported in this paper for a powder bed of micro metal particles under nanosecond laser pulse irradiation. In this study, ~200-ns laser pulses at the wavelength of ~1064 nm irradiate a powder bed of micro cobalt particles, and in-situ time-resolved temperature measurements have been conducted using a two-color pyrometry system. Under the conditions investigated in this paper, the discoveries listed below have been made:

- (1) The transient temperature history of the measurement spot on the powder bed surface predicted by the thermal model agrees reasonably well with that measured by the pyrometry system under the given condition.
- (2) The irradiation by ~200-ns-duration laser pulses at the 25 kHz pulse frequency has created a significant pulse-to-pulse thermal accumulation effect in the cobalt powder bed and a melt pool with an oscillating size. Such a thermal accumulation effect is not seen in the model simulation result for a bulk cobalt target even for 100 kHz nanosecond laser pulses, due to its much larger thermal conductivity.
- (3) With the same time-averaged laser power and total laser energy input, by changing the laser pulse frequency, the ~200-ns duration laser pulses can induce significantly different temperature histories, melt pool evolutions and lifetimes. They can either produce a relatively short-lasting melt pool with a very high transient peak temperature, or a more continuous and longer-lasting melt pool with a much lower peak temperature. This suggests that laser sintering

with a nanosecond laser is very adjustable and flexible, which is a potential great advantage. It also means a very complicated relation between laser parameters and thermal responses, which is a challenge in parameter selections, implying the importance and value of a thermal model validated by time-resolved temperature measurements.

(4) Compared with the powder bed of micro cobalt particles, the nanosecond laser pulse-induced thermal responses become much less complicated for a bulk cobalt target, which has a much higher thermal conductivity and thus little thermal accumulation effect even under a high laser pulse frequency of 100 kHz.

# **CRediT** authorship contribution statement

**Hanyu Song:** Data curation, formal analysis, investigation, methodology, software, validation, visualization, writing-original draft, writing-review and editing.

**Mengchen Wu:** Methodology, software, validation, formal analysis, investigation, data curation, writing-original draft, writing-review and editing, visualization.

Weidong Liu: Investigation, methodology, writing-review & editing

**Benxin Wu:** Conceptualization, formal analysis, funding acquisition, investigation, methodology, project administration, supervision, writing-original draft, writing-review and editing.

## **Declaration of Competing Interest**

The corresponding author, Benxin Wu, is the inventor of the following patent application on double-pulse laser micro sintering that has been filed: Inventor: Benxin Wu; assignee: Purdue Research Foundation, "*Processes and systems for double-pulse laser micro sintering*", United States patent application, application number: 16/427,638, filed on May 31<sup>st</sup> 2019 (the related provisional patent has an application number of 62693684 and was filed on July 3<sup>rd</sup> 2018).

## Acknowledgments

This material is based upon work supported by the National Science Foundation under Grant No. CMMI 1728481. The grantee university for this grant is Purdue University located at West Lafayette in the state of Indiana, USA.

## **List of References**

- 1. Kruth, J.P., Mercelis, P., Van Vaerenbergh, J., Froyen, L. and Rombouts, M., "Binding mechanisms in selective laser sintering and selective laser melting", Rapid Prototyping Journal, 11: 26-36, 2005.
- 2. Wang, Y., Shi, J., Lu, S. and Wang, Y., "Selective laser melting of graphene-reinforced Inconel 718 superalloy: evaluation of microstructure and tensile performance", Journal of Manufacturing Science and Engineering, 139: 041005, 2017.
- 3. Fischer, P., Locher, M., Romano, V., Weber, H.P., Kolossov, S. and Glardon, R., "Temperature measurements during selective laser sintering of titanium powder", International Journal of Machine Tools and Manufacture, 44(12-13):1293-1296, 2004.
- 4. Caprio, L., Demir, A.G. and Previtali, B., "Influence of pulsed and continuous wave emission on melting efficiency in selective laser melting", Journal of Materials Processing Technology, 266: 429-441, 2019.
- 5. Caprio, L., Demir, A.G. and Previtali, B., "Comparative study between CW and PW emissions in selective laser melting", Journal of Laser Applications, 30(3): 032305, 2018.
- 6. Chivel, Y. and Smurov, I., "On-line temperature monitoring in selective laser sintering/melting", Physics Procedia, 5: 515-521, 2010.
- 7. Smelov, V.G., Sotov, A.V. and Murzin, S.P., "Particularly selective sintering of metal powders by pulsed laser radiation", Key Engineering Materials, 685: 403-407, 2016.
- 8. Regenfuss, P., Streek, A., Hartwig, L., Klötzer, S., Brabant, Th., Horn, M., Ebert, R. and Exner, H., "Principles of laser micro sintering", Rapid Prototyping Journal, 13:204-212, 2007.
- 9. Streek, A., Regenfuss, P., Ebert, R. and Exner, H., "Laser micro sintering—a quality leap through improvement of powder packing", 2008 International Solid Freeform Fabrication Symposium.
- 10. Yin, J., Zhu, H., Ke, L., Hu, P., He, C., Zhang, H. and Zeng, X., "A finite element model of thermal evolution in laser micro sintering", The International Journal of Advanced Manufacturing Technology, 83(9-12):1847-1859, 2016.
- 11. Yin, J., Zhu, H., Ke, L., Lei, W., Dai, C. and Zuo, D., "Simulation of temperature distribution in single metallic powder layer for laser micro-sintering", Computational Materials Science, 53(1): 333-339, 2012.
- 12. Dayal, R., Gambaryan-Roisman, T. and Abele, E., "Numerical study of heat transfer and phase change in a single metal particle of powder material in application to selective laser sintering", Computational Thermal Sciences: An International Journal, 3(3): 169-177, 2011.
- 13. Fischer, P., Romano, V., Weber, H.P., Karapatis, N.P., Andre, C. and Glardon, R., "Modeling of near infrared pulsed laser sintering of metallic powders", In ALT'02 International Conference on Advanced Laser Technologies (5147: 292-298). International Society for Optics and Photonics, 2003.
- 14. Ye, C. and Cheng, G.J., "Numerical investigation of temperature field during sintering of bioceramic nanoparticles by pulse lasers", In International Manufacturing Science and Engineering Conference (48517: 263-273), 2008.

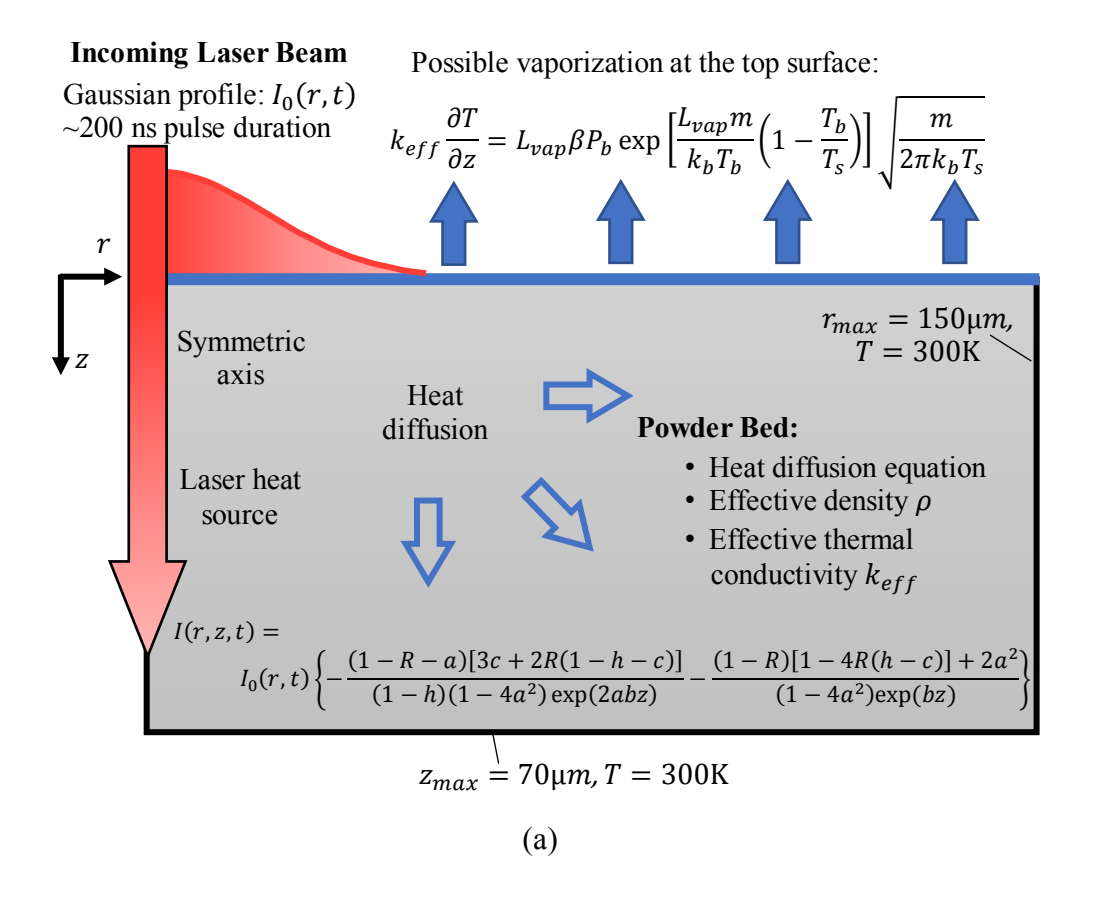
- 15. Cheng, C.W. and Chen, J.K., "Femtosecond laser sintering of copper nanoparticles", Applied Physics A, 122(4): 289, 2016.
- 16. Song, H., Kang, Z. and Wu, B., "Time-resolved in-situ temperature measurement and analysis for continuous-wave laser sintering of carbon nanotube–Metal composites on a polymer substrate", Journal of Manufacturing Processes, 66: 435-445, 2021.
- 17. Liu, W., Song, H., Wu, B. and You, H., "Double-pulse laser micro sintering: Experimental study and mechanism analysis aided by in-situ time-resolved temperature measurements", Journal of Manufacturing Processes, 69: 191-203, 2021.
- 18. Tao, S., Zhou, Y., Wu, B. and Gao, Y., "Infrared long nanosecond laser pulse ablation of silicon: integrated two-dimensional modeling and time-resolved experimental study", Applied Surface Science, 258:7766–7773, 2012.
- 19. Xiao, B. and Zhang, Y., "Marangoni and buoyancy effects on direct metal laser sintering with a moving laser beam", Numerical Heat Transfer, Part A: Applications, 51(8):715-33, 2007.
- 20. Gusarov, A.V. and Kruth, J.P., "Modelling of radiation transfer in metallic powders at laser treatment", International Journal of Heat and Mass Transfer, 48(16): 3423-3434, 2005
- 21. Ankudinov, V., Gordeev, G.A. and Krivilyov, M.D., "Numerical simulation of heat transfer and melting of Fe-based powders in SLM processing", In IOP Conference Series: Materials Science and Engineering (192(1): 012026), IOP Publishing, 2017.
- 22. The Iron Triad: Iron, Cobalt, and Nickel. (Last updated: August 25, 2020). Last accessed on August 28, 2021, from https://chem.libretexts.org/@go/page/24345
- 23. Thermal Properties of Metals, Conductivity, Thermal Expansion, Specific Heat. https://www.engineersedge.com/properties\_of\_metals.htm (last accessed on August 28, 2021).
- 24. Fleitman, A.H., Herchenroeder, R.B. and Chow, J.G.Y, "Cobalt-base alloys for use in nuclear reactors", Nuclear Engineering and Design, 15:345-62, 1971.
- 25. Materials Thermal Properties Database. https://thermtest.com/materials-database (last accessed on August 28, 2021).
- 26. Argon Thermophysical Properties. https://www.engineeringtoolbox.com/argon-d\_1414.html (last accessed on August 28, 2021)
- 27. Chen, S.H.P. and Saxena, S.C., "Thermal conductivity of argon in the temperature range 350 to 2500 K", Molecular Physics, 29(2): 455-466, 1975.
- 28. Smith, D.S., Alzina, A., Bourret, J., Nait-Ali, B., Pennec, F., Tessier-Doyen, N., Otsu, K., Matsubara, H., Elser, P. and Gonzenbach, U.T., "Thermal conductivity of porous materials", Journal of Materials Research, 28(17): 2260-2272, 2013.
- 29. Gusarov, A.V. and Smurov, I., "Thermal model of nanosecond pulsed laser ablation: Analysis of energy and mass transfer", Journal of Applied Physics, 97(1):014307, 2005.
- 30. Knight, C.J., "Transient vaporization from a surface into vacuum", AIAA Journal, 20(7): 950-4, 1982.
- 31. Miotello, A. and Kelly, R., "Critical assessment of thermal models for laser sputtering at high fluences", Applied Physics Letters, 67(24): 3535-7, 1995.

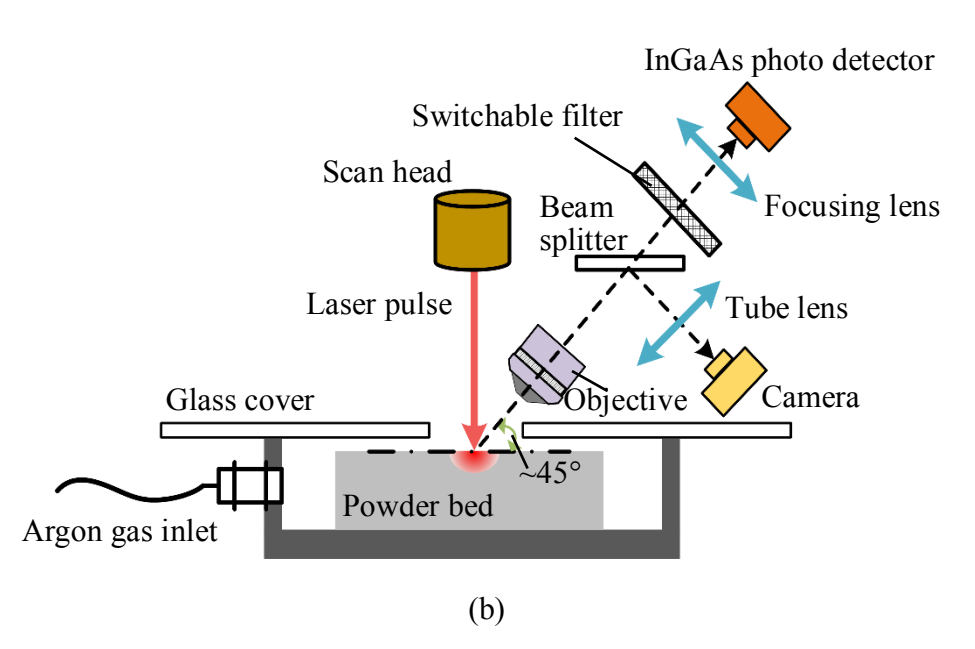
- 32. Schneider, C. A., Rasband, W.S. and Eliceiri, K.W., "NIH Image to ImageJ: 25 years of image analysis", Nature Methods 9(7): 671-675, 2012 (Also see: https://imagej.net/ImageJ1)
- 33. Sundqvist, H. and Veronis, G., "A simple finite-difference grid with non-constant intervals", Tellus, 22(1): 26-31, 1970.
- 34. Guillermet, A.F., "Critical evaluation of the thermodynamic properties of cobalt", International Journal of Thermophysics, 8(4): 481-510, 1987.
- 35. Li, Z., Bigdeli, S., Mao, H., Chen, Q. and Selleby, M., "Thermodynamic evaluation of pure Co for the third generation of thermodynamic databases", Physica Status Solidi (b), 254(2): 1600231, 2017.
- 36. Terada, Y., Ohkubo, K., Mohri, T. and Suzuki, T., "Thermal conductivity of cobalt-base alloys", Metallurgical and Materials Transactions, 34(9): 2026, 2003.
- 37. Assael, M.J., Antoniadis, K.D., Wakeham, W.A., Huber, M.L. and Fukuyama, H., "Reference correlations for the thermal conductivity of liquid bismuth, cobalt, germanium, and silicon", Journal of Physical and Chemical Reference Data. 46(3): 033101, 2017.
- 38. Yu, A.C., Donovan, T.M. and Spicer, W.E., "Optical properties of cobalt", Physical Review, 167(3): 670-673, 1968
- 39. Siegel, E., "Optical reflectivity of liquid metals at their melting temperatures", Physics and Chemistry of liquids, 5(1): 9-27, 1976.
- 40. Howell, John R., Mengüç, M. Pinar, and Siegel, Robert, Thermal Radiation Heat Transfer (6th Edition) 2. Radiative Properties at Interfaces, CRC Press, 2016.
- 41. Pedrotti, F. L., Pedrotti, L. S. and Pedrotti, L.M., Introduction to Optics, Pearson Prentice Hall, 2007.
- 42. Shibuta, Y. and Suzuki, T., "A molecular dynamics study of the phase transition in bcc metal nanoparticles", The Journal of chemical physics, 129(14): 144102, 2008.
- 43. Zhou, Y., Wu, B. and Forsman, A., "Time-resolved observation of the plasma induced by laser metal ablation in air at atmospheric pressure", Journal of Applied Physics, 108(9): 093504, 2010.
- 44. Wei, L.C., Ehrlich, L.E., Powell-Palm, M.J., Montgomery, C., Beuth, J. and Malen, J.A., "Thermal conductivity of metal powders for powder bed additive manufacturing", Additive Manufacturing, 21: 201-208, 2018.
- 45. Zhang, S., Lane, B., Whiting, J. and Chou, K., "On thermal properties of metallic powder in laser powder bed fusion additive manufacturing", Journal of manufacturing processes, 47: 382-392, 2019.
- 46. Incropera, F.P. and DeWitt, D.P., Fundamentals of Heat and Mass Transfer, John Wiley & Sons, 2002.
- 47. Williams, E. and Brousseau, E.B., "Nanosecond laser processing of Zr<sub>41.2</sub>Ti<sub>13.8</sub>Cu<sub>12.5</sub>Ni<sub>10</sub>Be<sub>22.5</sub> with single pulses", Journal of Materials Processing Technology, 232: 34-42, 2016.
- 48. Sinha, S., "Thermal model based simulation of nanosecond pulsed laser irradiation of Ti6Al4V alloy", Journal of Laser Applications, 31(3): 032008, 2019.

**Table 1.** Major properties applied in the calculations using the model [24, 27, 34-39]

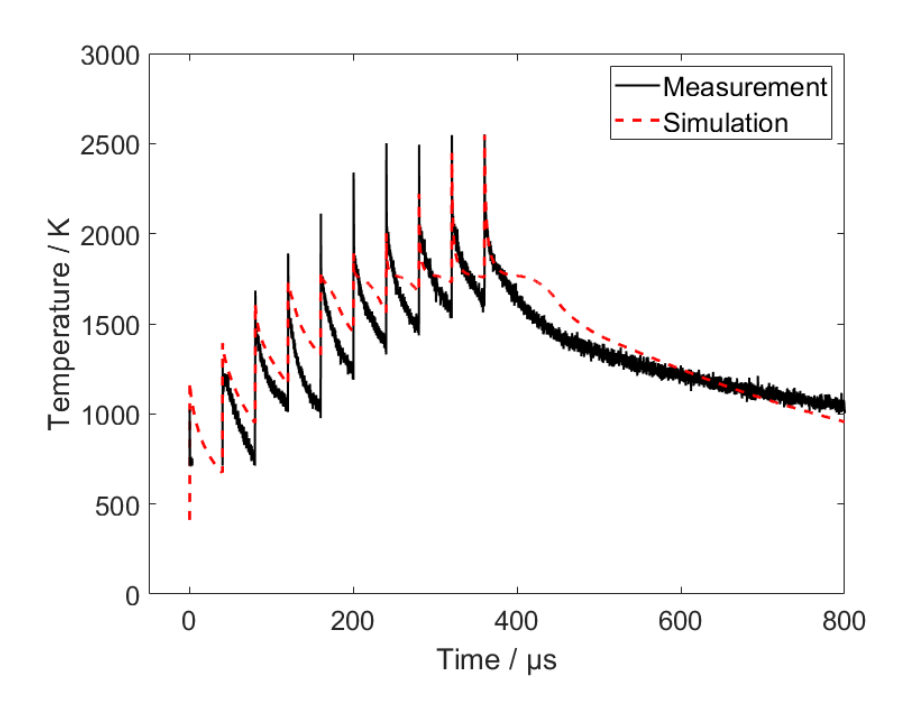
Property*	Symbol	Value or Source	Ref.
Melting temperature	$T_m$	1768 K (1495 °C in [24])	[24]
Boiling temperature	$T_b$	3173 K (2900 °C in [24])	[24]
Solid density	$ ho_{b,s}$	$8850 \text{ kg/m}^3$	[24]
Liquid density	$ ho_{b,l}$	$7750 \text{ kg/m}^3$	[34]
Melting latent heat	$L_m$	$5.84 \times 10^4$ cal/kg	[24]
Vaporization latent heat	$L_{vap}$	$1.5 \times 10^6$ cal/kg	[24]
Solid specific heat	$C_{p,s}$	Piecewise linear interpolations using values digitized from Fig. 2 (black curve, at the points of 298K, 695K) and Fig. 4 (at the points of 1150K, 1390K, 1460K, 1650K) of [35], as well as the $C_{p,l}$ value (40.5 J/(mol·K)) at $T_m$ .	[35]
Solid thermal conductivity	$k_{b,s}$	Based on Fig.3 of [36]	[36]
Liquid specific heat	$C_{p,l}$	40.5 J/(mol·K) (estimated based on Fig. 1 of [35])	[35]
Liquid thermal conductivity	$k_{b,l}$	Table 6 of [37] (for T<1800 K or T > 1950 K, the constant value at 1800 K or 1950 K is used, respectively, for liquid)	[37]
Solid complex refractive index	$\widetilde{n}_{\scriptscriptstyle S}$	Based on Fig. 6 of Ref. [38]	[38]
Liquid complex refractive index	$\widetilde{n}_l$	Based on Table III of Ref. [39]	[39]
Thermal conductivity for argon	$k_a$	Based on Table 1 of Ref. [27]	[27]

<sup>\*</sup>Unless indicated otherwise, the properties given in the table are for the bulk cobalt, based on which the determination of the effective properties of the powder bed medium (e.g., its effective density and thermal conductivity) are introduced in the text of this paper.

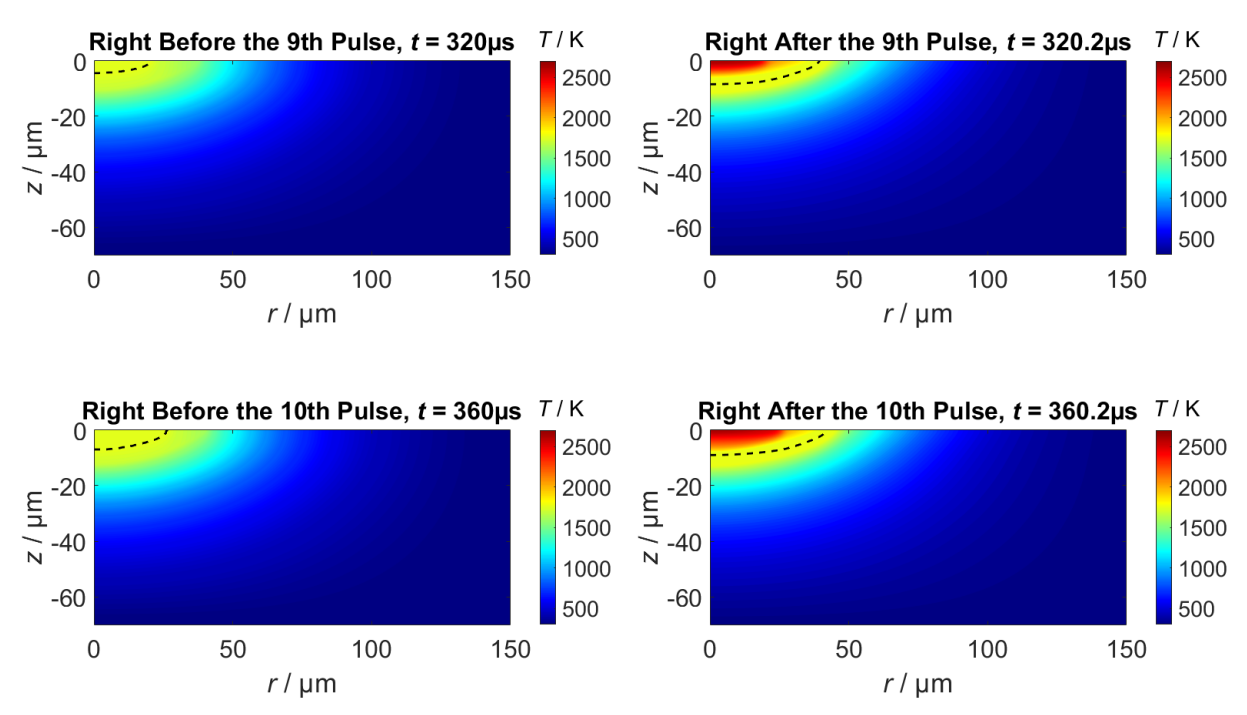




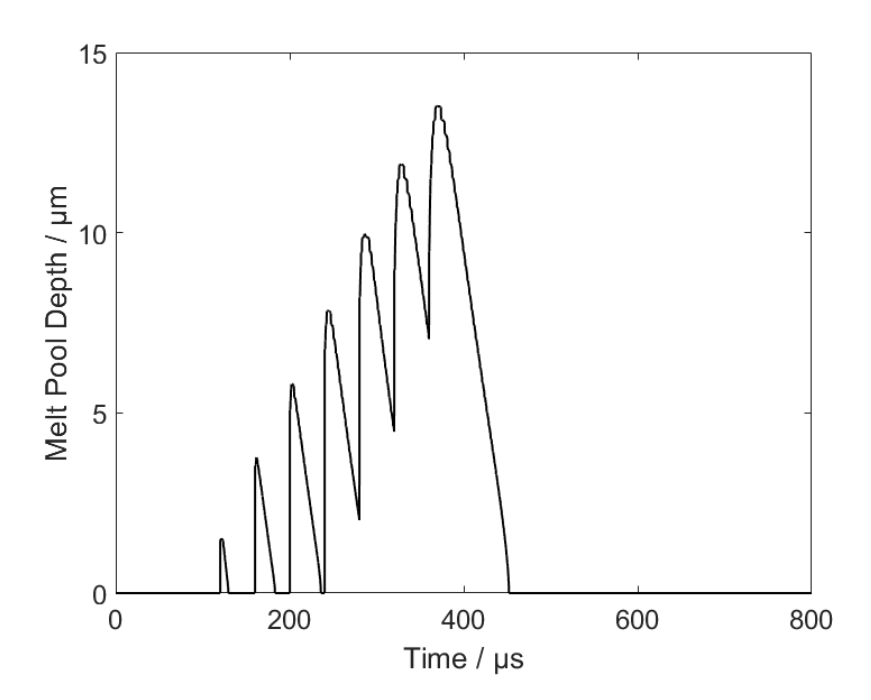
**Figure 1.** Schematic diagrams of: (a) the thermal model setup and (b) the experimental setup for nanosecond laser irradiation of a powder bed of micro metal particles, together with the pyrometry temperature measurement system (the schematics do not show all components of the setups and does not necessarily demonstrate things in an exact way).



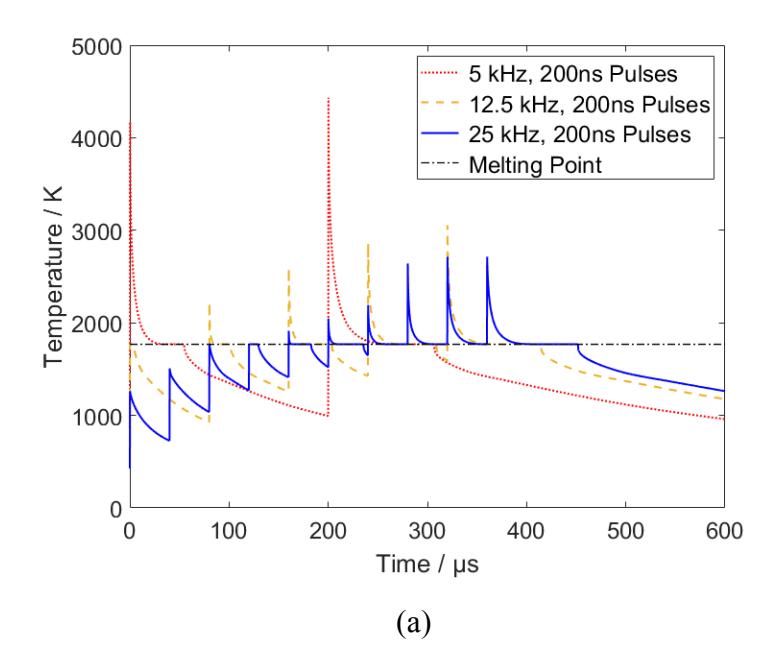
**Figure 2**. The model prediction versus the experimental result via the pyrometry system for the temperature history of the measurement spot on the cobalt powder bed surface (25 kHz pulse frequency, 10 laser pulses,  $\sim$ 0.14 mJ/pulse, and  $\sim$ 200-ns pulse duration; the first laser pulse starts at t = 0).



**Figure 3**. The model-predicted cross-sectional temperature contour plots for the powder bed at different moments (the laser parameters are the same as those for Fig.2; the starting moment of the  $1^{st}$  laser pulse is defined as t = 0; the dashed black line in each plot indicates the melt pool boundary).



**Figure 4**. The model-predicted history of the powder bed melt pool depth at the laser spot center (the laser parameters are the same as those for Fig.2).



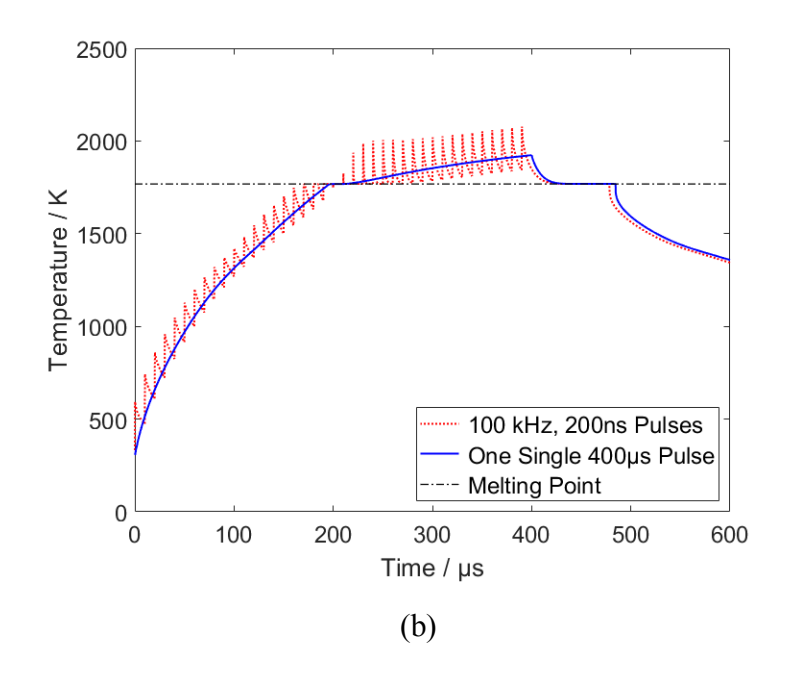


**Figure 5.** The model-predicted powder bed surface temperature history at the laser spot center induced by laser pulses fired in the period of t = 0 to 400  $\mu$ s with the same total laser energy input but different pulse frequencies: (a) two ~200-ns-duration laser pulses fired at 5 kHz, five pulses fired at 12.5 kHz, and ten pulses fired at 25 kHz; and (b) forty ~200-ns-duration laser pulses fired at 100 kHz and one single 400- $\mu$ s-duration pulse fired (the total incoming laser energy has the same value of 1.4 mJ in the period of t = 0 to 400  $\mu$ s for all the cases).

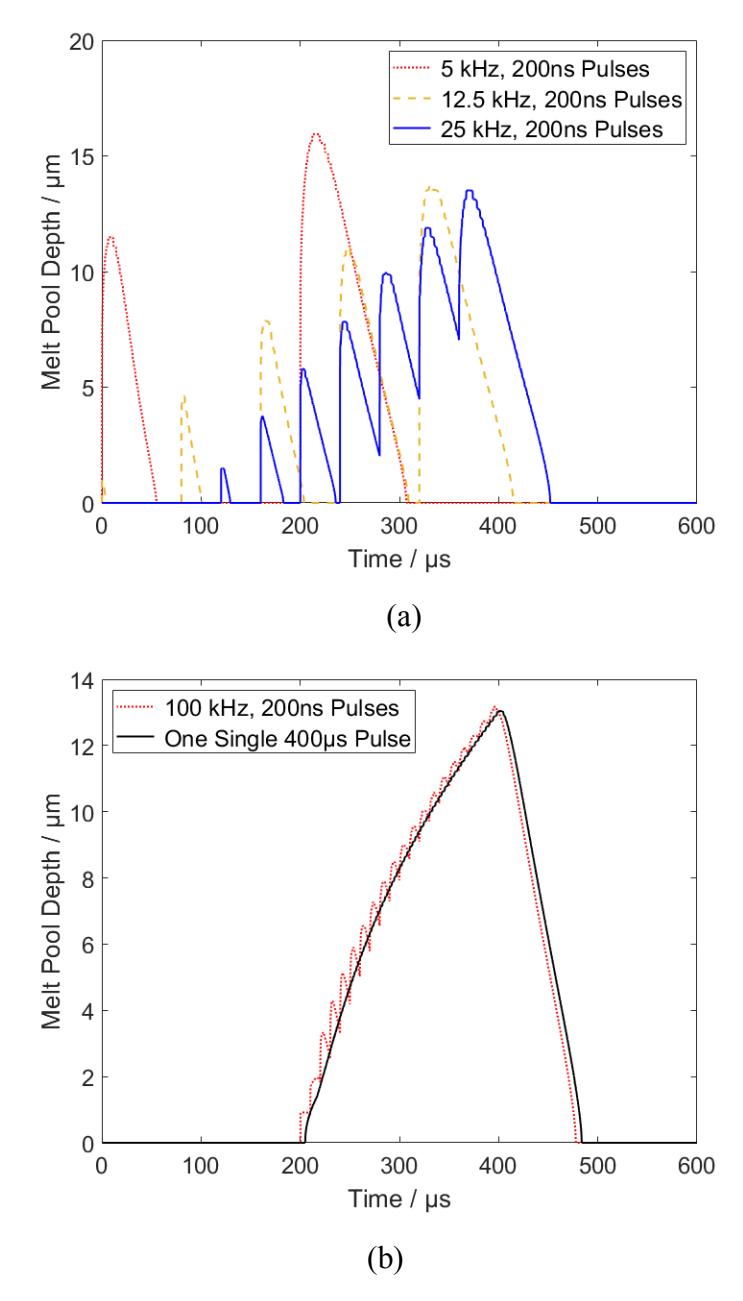


**Figure 6.** The model-predicted melt pool depths at the laser spot center for different laser pulse frequencies, where the laser conditions for (a) and (b) are the same as those for Fig. 5(a) and (b), respectively.

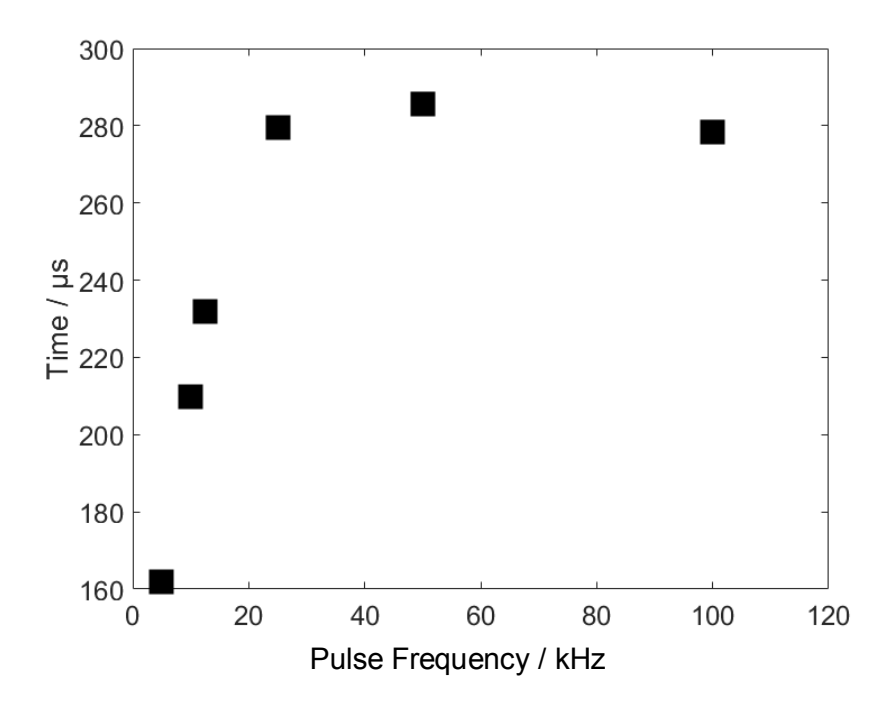


Figure 7. The model-predicted melt pool lifetimes in the powder bed induced by  $\sim 200$ -ns-duration laser pulses fired in the period of t=0 to  $400~\mu s$  with different laser pulse frequencies, but the same time-averaged laser power in the 400-us period (thus the same total laser energy input of 1.4 mJ).

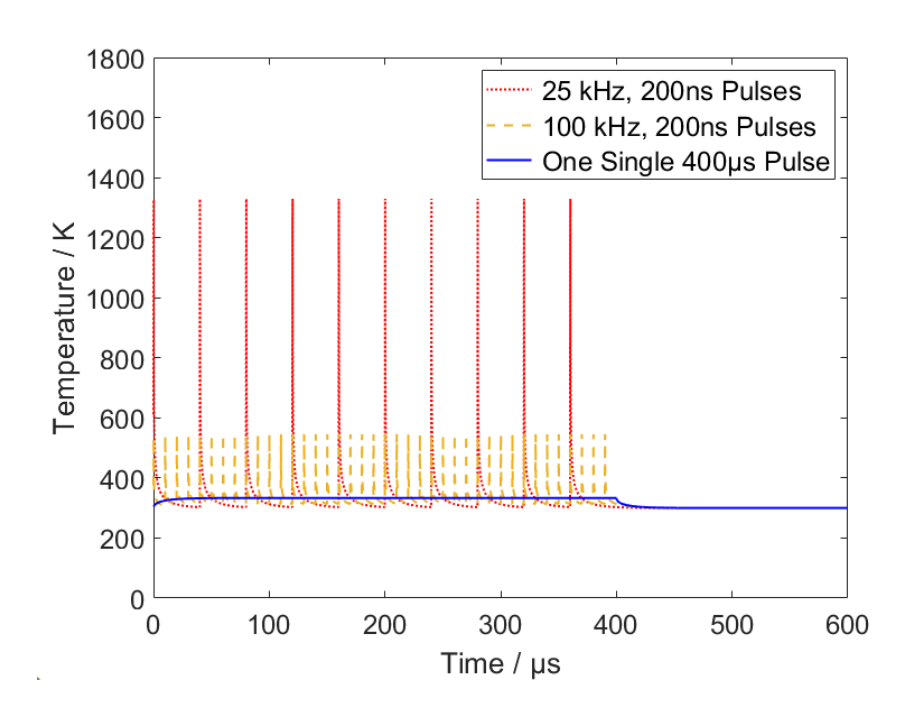


Figure 8. The model-predicted temperature history at the laser spot center for a bulk cobalt surface induced by: ten  $\sim$ 200-ns-duration pulses fired at 25 kHz, forty  $\sim$ 200-ns-duration pulses at 100 kHz and one 400- $\mu$ s-duration pulse (laser parameters are the same as those for the corresponding cases in Fig.5).